

Multifrequency VLBI observations of faint gigahertz peaked spectrum sources

I.A.G. Snellen^{1,2}, R.T. Schilizzi^{2,3}, H.J. van Langevelde³,

¹*Institute of Astronomy, Madingley Road, Cambridge CB3 0HA, United Kingdom*

²*Leiden Observatory, P.O. Box 9513, 2300 RA, Leiden, The Netherlands*

³*Joint Institute for VLBI in Europe, Postbus 2, 7990 AA, Dwingeloo, The Netherlands*

ABSTRACT

We present the data and analysis of VLBI observations at 1.6, 5 and 15 GHz of a sample of faint Gigahertz Peaked Spectrum (GPS) sources selected from the Westerbork Northern Sky Survey (WENSS). The 5 GHz observations involved a global array of 16 stations and yielded data on the total sample of 47 sources. A subsample of 26 GPS sources with peak frequencies $\nu_p > 5$ GHz and/or peak flux densities $S_p > 125$ mJy was observed with the VLBA at 15 GHz. A second subsample of 29 sources, with $\nu_p < 5$ GHz, was observed at 1.6 GHz using a 14 station global VLBI array. In this way, 44 of the 47 sources (94%) in the sample were observed above and at or below their spectral peak. Spectral decomposition allowed us to identify 3, 11, 7, and 2 objects as compact symmetric objects, compact doubles, core-jet and complex sources respectively. However, many of the sources classified as compact double or core-jet sources show only two components making their classification rather tentative. This may explain why the strong morphological dichotomy of GPS quasars and galaxies found for radio-bright GPS sources, is not as clear in this faint sample.

1 INTRODUCTION

Gigahertz Peaked Spectrum (GPS, e.g. O’Dea 1998) are a class of extragalactic radio source, characterised by a convex shaped radio spectrum peaking at about 1 GHz in frequency, and sub-galactic sizes. Their small sizes make observations using Very Long Baseline Interferometry (VLBI) necessary to reveal their radio morphologies. Early VLBI observations showed that some GPS sources identified with galaxies have Compact Double (CD) morphologies (Philips and Mutel, 1982), and it was suggested that these were the mini-lobes of very young or alternatively old, frustrated objects (Philips and Mutel, 1982; Wilkinson et al. 1984, van Breugel, Miley and Heckman, 1984). Later, when reliable VLBI observations at higher frequencies became possible, it was found that some of the CD-sources had a compact flat spectrum component in their centres (Conway et al. 1992, Wilkinson et al. 1994). These flat spectrum components were interpreted as the central cores, and many CD-sources were renamed compact triples or Compact Symmetric Objects (CSO, Conway et al. 1992, Wilkinson et al. 1994). High dynamic range VLBI observations by Dallacasa et al (1995) and Stanghellini et al. (1997) have shown that most GPS galaxies indeed have jets leading from the central compact core to the outer hotspots or lobes. This is in contrast to the GPS sources identified with quasars, which tend to have core-jet morphologies with no outer lobes (Stanghellini et al. 1997). Snellen et al. (1999) have shown that the redshift distributions of the GPS galaxies and quasars are very different, and that it is therefore unlikely that they form a

single class of object unified by orientation. They suggest that they are separate classes of object, which just happen to have the same radio-spectral morphologies.

The separation velocities of the hotspots have now been measured for a small number of GPS galaxies to be $0.2h^{-1}c$ (Owsianik and Conway, 1998; Owsianik, Conway and Polatidis, 1998; Tschager et al. 1999). This makes it very likely that these are young objects of ages typically $\sim 10^3$ yr (assuming a constant separation velocity), rather than old objects constrained in their growth by a dense ISM. These are therefore the objects of choice to study the early evolution of extragalactic radio sources.

In the past, work has been concentrated on samples of the radio brightest GPS sources (eg. O’Dea et al 1991). In order to disentangle radio power and redshift effects on the properties of GPS sources, we constructed a sample of faint GPS sources from the Westerbork Northern Sky Survey (WENSS, Rengelink et al. 1997), which in combination with other samples allows, for the first time, the study of these objects over a large range of flux density and radio spectral peak frequency. The construction of the faint sample is described in Snellen et al. (1998a); the optical and near-infrared imaging is described in Snellen et al. (1998b); and the optical spectroscopy in Snellen et al. (1999a). This paper describes multi-frequency VLBI observations of the sample, and the radio-morphologies of the individual sources. What can be learned from the faint GPS sample about radio source evolution is discussed in the accompanying paper (Snellen et al. 2000).

2 THE SAMPLE

The selection of the sample has been described in detail in Snellen et al. (1998a), and is summarised here. Candidate GPS sources were selected from the Westerbork Northern Sky survey, by means of an inverted spectrum between 325 MHz and higher frequencies. The sources are located in two regions of the survey; one with $15^h < \alpha < 20^h$ and $58^\circ < \delta < 75^\circ$, which is called the *mini-survey* region (Rengelink et al. 1997), and the other with $4^h00^m < \alpha < 8^h30^m$ and $58^\circ < \delta < 75^\circ$. Additional observations at 1.4, 5, 8.4 and 15 GHz were carried out with the WSRT and the VLA, yielding a sample of 47 genuine GPS sources with peak frequencies ranging from 500 MHz to more than 15 GHz, and peak flux densities ranging from ~ 30 to ~ 900 mJy. This sample has been imaged in the optical and near-infrared, resulting in an identification fraction of $\sim 87\%$ (Snellen et al. 1998b). Redshifts have been obtained for 40% of the sample (Snellen et al., 1999).

3 OBSERVATIONS

Snapshot VLBI observations were made of the entire sample of faint GPS sources at 5 GHz, and of sub-samples at 15 GHz and 1.6 GHz frequency. In order to observe the large number of sources required in a reasonable amount of time, we observed in “snapshot” mode (eg. Polatidis et al. 1995, Henstock et al. 1995). This entails observing a source for short periods of time at several different hour angles. Using a VLBI array of typically more than 10 telescopes, this provides sufficient u, v coverage for reliable mapping of complex sources (Polatidis et al. 1995). To maximize the u, v coverage for each source we attempted to schedule three to four scans as widely spaced as possible within the visibility window during which the source could be seen by all antennas. Fortunately, the majority of the sources are located at a sufficiently high declination ($> 57^\circ$) that they are circumpolar for most EVN and VLBA antennas, and therefore could be scheduled for observation at optimal hour angles.

3.1 The 5 GHz Observations, Correlation and Reduction

The 5 GHz data were obtained during a 48 hour observing session on 15 and 16 May 1995. All telescopes of the VLBA, and six telescopes of the EVN were scheduled to participate in this global VLBI experiment (see table 1). The data were recorded using the Mark III recording system in mode B, with an effective bandwidth of 28 MHz centred at 4973 MHz. Left circular polarization was recorded. Since the motion of some of the antennas is limited in hour angle, we inevitably had to schedule a few scans when the source could not be observed at one or two telescopes. All sources were observed for three scans of 13 minutes (13^m corresponds to a single pass on a tape).

The data were correlated using the VLBA correlator in Socorro, New Mexico, four months after the observations took place. The output of the correlator provides a measure of the complex fringe visibility sampled at intervals of 2 seconds on each baseline, at 7×16 frequencies within the 28 MHz band, with the phase referenced to an *a priori* model

of the source position, antenna locations, and atmosphere. The residual phase gradients in time and frequency due to delay and rate errors in the *a priori* model are estimated and removed, during the process of “fringe fitting”. Fringe fitting was performed using the AIPS task FRING, an implementation of the Schwab & Cotton (1983) algorithm. A solution interval of 3 minutes and a point source model were used, and Effelsberg was taken as the “reference telescope” whenever possible. No fringes were found for the Cambridge telescope. The amplitude calibration was performed with the AIPS tasks ANTAB and APCAL, using system temperature and antenna gain information. The visibility data were averaged across the observing band and then written in one single u, v -file per object. The typical u, v coverage obtained for a source is shown in figure 1.

The final images were produced after several cycles of imaging and self-calibration using the AIPS tasks IMAGR and CALIB. Solution intervals were decreased in each step, starting with a few minutes, until no increase of the image quality (using noise-level and the presence of negative structure as criteria) was detected. If a source was sufficiently strong, antenna amplitude solutions were also determined for each scan. For each source a “natural” weighted image was produced. If the u, v -data were of sufficient quality, a “uniform” weighted image was also produced.

3.2 The 15 GHz Observations, Correlation and Reduction

The 15 GHz data were obtained during a 24 hour observing session on 29 June 1996, using the ten telescopes of the VLBA. The data were recorded in 128 – 8 – 1 mode (128 Mbits/sec, 8 IF channels, 1 bit/sample), with an effective bandwidth of 32 MHz centred at 15360 MHz. All 27 sources in the sample with peak frequencies higher than 5 GHz and/or peak flux densities greater than 125 mJy were observed. The expected maximum brightness in each of the images at 15 GHz was estimated from the overall radio spectra of the sources and their 5 GHz VLBI morphology. In order to use the conventional fringe-fitting methods of VLBI imaging, the signal to noise ratio on each baseline within the coherence time has to be sufficiently high. Sources with an expected maximum brightness at 15 GHz of > 60 mJy/beam are sufficiently strong and were observed for 3 scans of 11 minutes each. However, sources with expected maximum brightnesses of < 60 mJy/beam, were observed using a “phase-referencing” method to increase the signal to noise ratio. This involves observations of the target source interspersed with observations of a nearby ($< 2.5^\circ$) compact calibrator source. Measurements of residual delay and rate are made towards this bright source and transferred to the target source data. We used cycles of 3 minutes on the target source and 1.5 minutes on the calibrator source. The total integration time on a target was 45 minutes divided over three scans. The sources for which the phase referencing technique was required and the calibration sources used (in brackets) were B0400+6042 (B0354+599), B0436+6152 (B0444+634), B0513+7129 (B0518+705), B0531+6121 (B0539+6200), B0538+7131 (B0535+6743), B0755+6354 (B0752+6355), B1525+6801 (B1526+670), B1538+5920 (B1550+5815), B1600+7131 (B1531+722), B1819+6707 (B1842+681), and B1841+6715 (B1842+681). Data reduction of the phase

Telescope	Location	Diam. (m)	SEFD _{1.6GHz} (Jy)	SEFD _{5GHz} (Jy)	SEFD _{15GHz} (Jy)
Cambridge	EVN, U.K.	32		136	
Effelsberg	EVN, Germany	100	19	20	
JB, Lovell	EVN, U.K.	76	44		
JB, MK2	EVN, U.K.	25		320	
Medicina	EVN, Italy	32		296	
Noto	EVN, Italy	32		260	
Torun	EVN, Poland	32	230		
Westerbork	EVN, Netherlands	12 × 25	450*	90	
VLBA_BR	Brewster, WA, USA	25	300	300	525
VLBA_FD	Fort Davis, TX, USA	25	300	300	525
VLBA_HN	Hancock, NH, USA	25	300	300	525
VLBA_KP	Kitt Peak, AZ, USA	25	300	300	525
VLBA_LA	Los Alamos, NM, USA	25	300	300	525
VLBA_MK	Mauna Kea, HI, USA	25	300	300	525
VLBA_NL	North Liberty, IA, USA	25	300	300	525
VLBA_OV	Owens Valley, CA, USA	25	300	300	525
VLBA_PT	Pie Town, NM, USA	25	300	300	525
VLBA_SC	Saint Croix, VI, USA	25	300	300	525

* Westerbork only observed with a single antenna at 1.6 GHz.

Table 1. The telescopes used for the VLBI observations

referenced observations is similar to that for the 5 GHz data. The typical u, v coverage obtained for a source at 15 GHz is shown in figure 1.

3.3 The 1.6 GHz Observations, Correlation and Reduction

The 1.6 GHz data were obtained during two observing sessions, both involving the ten telescopes of the VLBA and 4 antennas of the EVN (see table 1). The Westerbork data in the second session was lost due to technical failure. The data were recorded in 128 – 4 – 2 mode (128 Mbits/sec, 4 IF channels, 2 bit/sample), with an effective bandwidth of 32 MHz centred at 1663 MHz and 1655 during the first and second session respectively. In the first session, a subsample of 23 objects was observed for 2×12 hours on 14 and 16 September 1997. This subsample contained all sources with peak frequencies < 5 GHz, which were found to be extended in the 5 GHz observations. In the second session, all 9 remaining sources with peak frequencies < 3 GHz, which had not been imaged before at this frequency, were observed. The sources were typically observed for 4×11 minutes each, and an example of a u, v coverage is shown in figure 1. The data were correlated in Socorro. No fringes were found for B0513+7129, B0537+6444, and B0544+5847. Several sources in the second session were observed using phase referencing. These sources, with their calibrators in brackets, are B0537+6444 (B0535+677), B0830+5813 (B0806+573), B1557+6220 (B1558+595), B1639+6711 (B1700+685), and B1808+6813 (B1749+701). The data were reduced in a similar way as the data at 5 GHz.

4 RESULTS

The parameters of the resulting 102 images (29 at 1.6 GHz, 47 at 5 GHz, and 26 at 15 GHz) are given in table 2. Figure 2 shows the rms noise as function of the peak brightness in the images at the three observing frequencies. The dynamic ranges (defined as the ratio of the maximum brightness in the image to the rms noise in an area of blank sky) are between 125 and 2500 at 1.6 GHz, between 25 and 1700 at 5 GHz, and between 30 and 500 at 15 GHz. At 1.6 GHz, two of the bright sources have higher rms-noise levels than expected, which may indicate that the dynamic range is not limited by the thermal noise. To be able to compare the VLBI observations of this faint sample with those on bright GPS samples, it is important to determine whether components have been missed due to the limited dynamic range for this faint sample. We therefore plotted the distribution of dynamic range for the observations closest in frequency to the spectral peak (Fig. 3). Only 2 objects (B0755+6354 and B0544+5847) turn out not to have an image with a dynamic range > 100 .

In Figure 4 the ratio of total VLBI flux density in the images to the flux density in the NVSS at 1.6 GHz, to the MERLIN observations at 5 GHz, and to the VLA 15 GHz flux densities (from Snellen et al. 1998a), are plotted. This enables us to judge whether substantial structure has been resolved out in the VLBI observations. At 1.6 GHz, typically 90% of the NVSS flux density is recovered in the VLBI observations, while at 5 GHz the distribution peaks at 100%. Only at 15 GHz is the distribution much broader and peaks at about 80% of the flux density in the VLA observations, and hence provides some evidence that at this frequency some extended structure may be missed. The broadness of the peak is probably also influenced by variability.

Figures 5, 6, 7 give the maps of the individual sources with observations at three, two and one frequency respec-

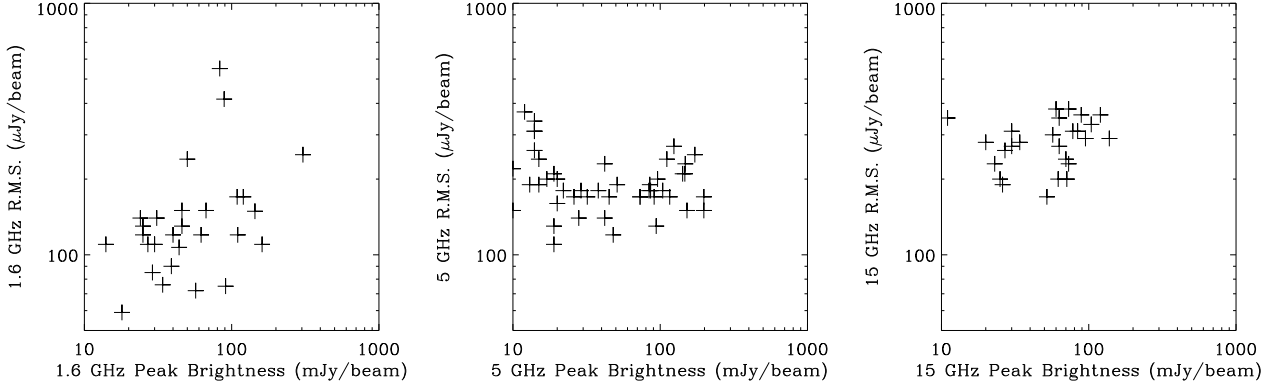


Figure 2. The rms noise levels as function of peak brightness for the 1.6, 5 and 15 GHz images.

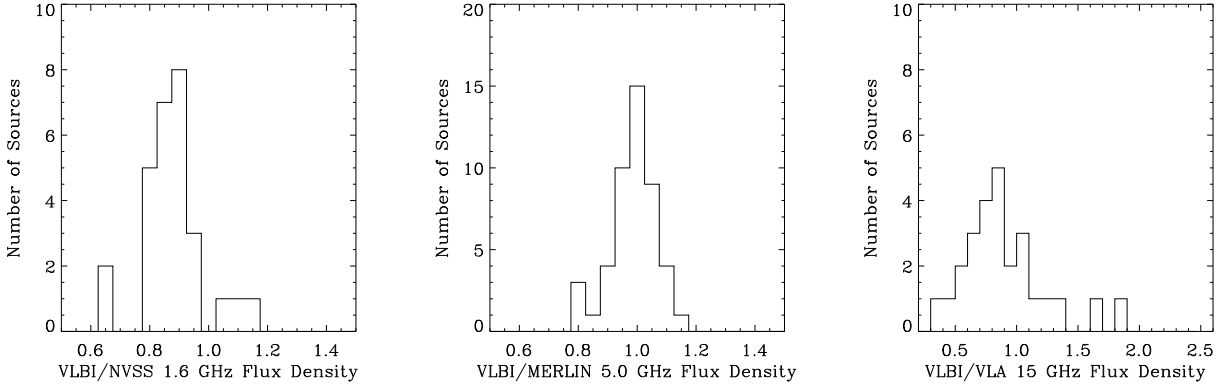


Figure 4. The ratio of total VLBI flux density in the maps to the flux density in the NVSS at 1.6 GHz (left), to the MERLIN observations at 5 GHz (middle), and to the VLA 15 GHz flux densities (right).

tively. For each source, the images have the same size at each frequency, and are centred in such a way that identical components at different frequencies match in relative position.

4.1 Model Fitting

Quantitative parameters of the source brightness distributions were estimated by fitting elliptical Gaussian functions to the maps, using the AIPS-task JMFIT. For some of the complex sources it was necessary to restrict the fit to a number of point sources (e.g. 0513+7129 at 5 GHz). In a few cases, the positions of some of the fitted components were kept fixed to correspond to their positions at higher frequency (e.g. 0752+6355 at 5 GHz). We checked whether the model was a good representation of the source structure, by comparing the total flux density in the image to that in the model, and by ensuring that the residual image did not show any significant negative structure. A spectral decomposition was performed by matching the components believed to correspond to each other at the different frequencies. Due to the increase in resolution with frequency, some components at the higher frequencies were combined to match a single component at the lower frequency. The decomposed spectra are

shown along with the images in figures 5 and 6. The results of the fits are given in table 3.

Column 1 gives the source name, column 2 the figure in which the maps are shown, and in column 3 the component name used for the spectral decomposition. Columns 4 to 8 give for each component observed at 1.6 GHz the flux density, relative position in R.A. and Dec., and the fitted angular size (major and minor axis, and position angle). Columns 9 to 13, and columns 14 to 18 give the same for the components observed at 5 GHz and 15 GHz respectively.

4.2 Classification of the Radio Morphologies

We classify the radio morphologies in four ways:

- 1) **Compact Symmetric Objects (CSO)**. Sources with a compact flat spectrum component with extended components with steeper spectra on either side.
- 2) **Core-Jet sources (CJ)**. Sources with compact flat spectrum component with one or more components with steeper spectra on one side only.
- 3) **Compact Double (CD)**. Sources showing two dominant components with comparable spectra, but no evidence of a central flat spectrum component.

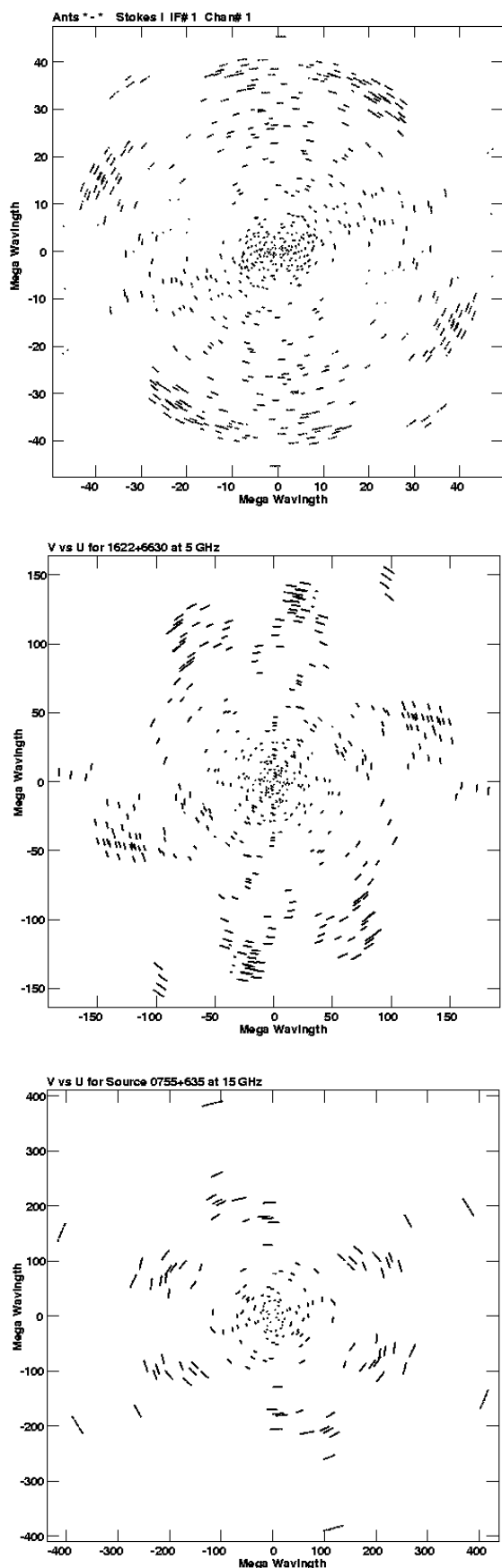


Figure 1. Typical u, v coverages for a source observed at 1.6 GHz (upper), 5 GHz (middle), 15 GHz (lower).

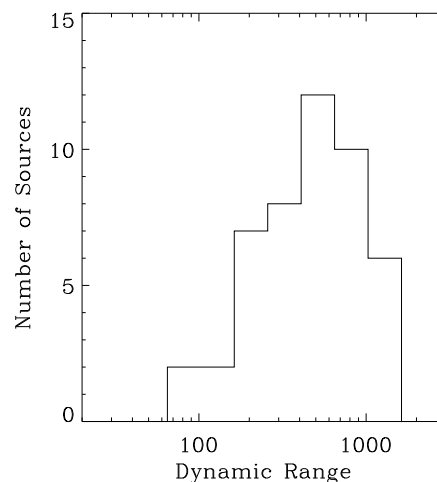


Figure 3. The dynamic ranges for all sources in the sample at the observed frequency closest to their spectral peak.

4) **Complex sources (CX)**. Sources with a complex morphology, not falling in one of the above categories.

From the 47 sources in the sample, 3 could be classified as CSO, 11 as CD, 7 as CJ, and 2 as CX. Of the 25 remaining sources, 2 were resolved at only one frequency, 2 were only observed at one frequency, and 20 show a single component at 2 frequencies, and therefore could not be classified. For one source (1642+6701) it was not clear how to overlay the 1.6 and 5 GHz maps. The individual sources are briefly discussed below.

4.2.1 Discussion of Individual Sources

B0400+6042: CD Several components are visible with the two outer components having comparable spectra and the central component having a marginally flatter spectrum. This source is tentatively classified as a CD, but it could also be a CSO.

B0436+6152: CSO The brightest component at 15 GHz in the centre is interpreted as the core, with extended steeper spectrum components to the north-east and south-west. This source is classified as a CSO.

B0441+5757: - Only one component is visible at both 5 and 15 GHz, therefore no classification was possible.

B0513+7129: CX This object shows two dominant components with a jet-like feature pointed to the north-west. Although the component with the flattest spectrum is located in the center, this source is classified as a complex source due to the strangely bent structure.

B0531+6121: - Only one component is visible at both 5 and 15 GHz, therefore no classification was possible.

B0535+6743: - Only one component is visible at 1.6, 5 and 15 GHz, therefore no classification was possible.

B0538+7131: - Only one component is visible at both 5 and 15 GHz, therefore no classification was possible.

B0537+6444: - This object was not resolved at 1.6 GHz and therefore no classification was possible.

B0539+6200: CJ The south-western component has a flatter spectral index than the north-eastern component. Only

two components are visible, hence this object is tentatively classified as a CJ.

B0543+6523: - The resolution at 1.6 GHz is not sufficient to make a spectral decomposition for the two components visible at 5 GHz. No classification was possible.

B0544+5847: - This object was observed only at 5 GHz, and therefore no classification was possible.

B0552+6017: - Only one component is visible at both 1.6 and 5 GHz, therefore no classification was possible.

B0557+5717: **CJ** The southern component has a flatter spectral index than the northern extended component. This object is classified as a core-jet.

B0601+5753: - Only one component is visible at both 5 and 15 GHz, therefore no classification was possible.

B0748+6343: - This object was observed only at 5 GHz, and therefore no classification was possible.

B0752+6355: **CX** The “C” shaped morphology of this compact source showing components with a large range of spectral indices, leads us to classify this object as one with a complex morphology.

B0755+6354: - Only one component is visible at both 5 and 15 GHz, therefore no classification was possible.

B0756+6647: - Only one component is visible at both 5 and 15 GHz, therefore no classification was possible.

B0758+5929: **CD** Two components are visible in this source, with more or less comparable spectra. We tentatively classify this object as a CD.

B0759+6557: **CD** This object has two component with similar spectra. This object is therefore classified as a CD.

B0826+7045: - This object was observed only at 5 GHz, and therefore no classification was possible.

B0830+5813: - This object shows only one component at both 1.6 and 5 GHz. Therefore no classification was possible.

B1525+6801: **CD** This source has two components with similar steep spectra. No core is found and this source is classified as a CD.

B1538+5920: - This source shows only one component at both 5 and 15 GHz. It is therefore not possible to classify this source.

B1550+5815: - This source shows only one component at both 5 and 15 GHz. It is therefore not possible to classify this source.

B1551+6822: - The resolution at 1.6 GHz is not sufficient to disentangle the individual spectra of the two components visible at 5 GHz. It is therefore not possible to classify this source.

B1557+6220: - This object was observed only at 5 GHz, and therefore no classification was possible.

B1600+7131: **CD** The two outermost structures have comparable steep spectra. This source is therefore classified as a CD.

B1620+6406: **CD** The steep spectrum of the northern component is similar to the spectrum of the southern component (using the upper-limit for the flux density at 5 GHz). We therefore tentatively classify this object as a CD.

B1622+6630: - This source shows only one component at both 5 and 15 GHz. It is therefore not possible to classify this source.

B1639+6711: - This source shows only one component at both 1.6 and 5 GHz. It is therefore not possible to classify this source.

B1642+6701: - It was not possible to reliably overlay the

two maps at 1.6 and 5 GHz, but the most likely match is shown in figure 6. Due to this uncertainty, it was not possible to reliably classify this source.

B1647+6225: **CD** The two components have similar spectra, with a possible jet leading to the northern component. This object is tentatively classified as a CD.

B1655+6446: **CD** Only the southern component is detected at 5 GHz. However its steep spectral index, and the upper-limit to the spectral index of the northern component makes us tentatively classify this source as a CD.

B1657+5826: **CD** Only the western component is detected at 5 GHz. However its steep spectral index, and the upper-limit to the spectral index of the eastern component makes us classify this source as a CD.

B1746+6921: **CJ** This source has a clear extension to the south east which has a steeper spectral index than the bright component. This source is therefore classified as a core-jet.

B1807+5959: **CJ** Three aligned components are visible at 1.6 and 5 GHz, from which the southern one is the brightest and has the flattest spectral index. This object is classified as a Core-jet.

B1807+6742: **CJ** The two components in this source have clearly different spectral indices. It is therefore classified as a CJ.

B1808+6813: - This source shows only one component at both 1.6 and 5 GHz. It is therefore not possible to classify this source.

B1819+6707: **CSO** Two dominant components are visible in this source at 1.6, 5, and 15 GHz with comparable spectra. A faint compact component is visible in between in the 5 GHz map. This object is therefore classified as a CSO.

B1841+6715: **CD** This object has two components with similar spectral indices, and is classified as a CD.

B1843+6305: **CD** This source has two components with similar spectral indices, and is tentatively classified as a CD.

B1942+7214: **CJ** This object shows faint extended structure to the south-west in its 1.6 and 5 GHz images. The bright northern component appears to have a flatter spectrum than the faint extended emission. We tentatively classify this object as a core-jet.

B1945+6024: - Only one component is detected at 5 and 15 GHz. It is therefore not possible to classify this source.

B1946+7048: **CSO** This source is the archetype compact symmetric object (CSO), and has been discussed in detail by Taylor and Vermeulen (1997). The core is only visible at 15 GHz.

B1954+6146: **CJ** Only the flat spectrum compact component in the south is detected at 15 GHz. The limit to the spectral index of the northern component makes us tentatively classify this source as a core-jet.

B1958+6158: - Only one component is detected at 5 and 15 GHz. It is therefore not possible to classify this source.

5 DISCUSSION

In radio bright samples, GPS quasars are found to have core-jet or complex structure, while GPS galaxies are found to have larger sizes with jets and lobes on both sides of a putative center of activity (Stanghellini et al. 1997). Although observations at another frequency are needed to confirm their classification, almost all radio-bright GPS galax-

ies from Stanghellini et al (1997) can be classified as CSOs. The morphological dichotomy of GPS galaxies and quasars, and their very different redshift distributions make it likely that GPS galaxies and quasars are not related to each other and just happen to have similar radio spectra. It has been speculated that GPS quasars are a subset of flat spectrum quasars in general (eg. Snellen et al. 1999a). In addition, if galaxies and quasars were to be unified by orientation, due to changes in its observed radio spectrum (Snellen et al. 1998c), it is not expected that a GPS galaxy observed at a small viewing angle would be seen as a GPS quasar.

Not all CSOs are GPS sources. The contribution of the (possibly variable) flat spectrum core can be significant and outshine the convex spectral shape produced by the mini-lobes. This can be due to a small viewing angle towards the object, causing the Doppler boosted core and fast moving jet, which feeds the approaching mini-lobe, to be important (Snellen et al. 1998c). An example of such a CSO, possibly observed at a small viewing angle, is 1436+135 (Perlman et al. 1994). In addition, the jets feeding the mini-lobes can be significantly curved, for example in 2352+495 by precession (Readhead et al. 1996). This can cause parts of the jet to move at an angle close to the line of sight, with significant Doppler boosting as a result. In both cases the large contrast between the approaching and receding parts of the radio source makes it also increasingly difficult to identify the object as a CSO.

Figure 8 shows the number of galaxies and quasars, in our faint GPS sample, classified as CJ, CSO, CX and those not possible to classify. All three objects classified as CSOs are optically identified with galaxies. Although this is in agreement with the findings of Stanghellini et al (1997) for the radio-bright sample, it should be noted that for only 4 quasars was it possible to make a classification. This is mainly due to the fact that the angular sizes of the quasars are significantly smaller than the angular sizes of the galaxies. Six out of 18 classifiable GPS galaxies are found to have CJ or CX structures, and 9 of the classifiable GPS galaxies are found to have CD structures. We conclude that the strong strong morphological dichotomy between GPS galaxies and quasars found by Stanghellini (1997) in the bright GPS sample, is not as strong in this faint sample. Note, however, that the classification for the majority of the CJ and CD sources is based on two components and their relative spectral indices only. This makes their classification rather tentative. Firstly, a CD source could be erroneously classified as a CJ source due to a difference in the observed age between the approaching and receding lobe, causing a difference in observed radio spectrum of the two lobes. For a separation velocity of 0.4c, as observed for radio bright GPS galaxies (Owsianik and Conway 1998; Owsianik, Conway and Polatidis 1998), such an age difference can be as large as 30%. Secondly, differences in the local environments of the two lobes can also influence the spectra of the two lobes, resulting in an erroneous classification as core-jet. For example, if only the two lobes had been visible, B1819+6707 (fig 6) could have been mistaken for a core-jet source, since the spectral index of the eastern lobe is flatter than that of the western lobe.

6 CONCLUSIONS

Multi-frequency VLBI observations have been presented of a faint sample of GPS sources. All 47 sources in the sample were successfully observed at 5 GHz, 26 sources were observed at 15 GHz, and 20 sources were observed at 1.6 GHz. In this way 94% of the sources have been mapped above and below their spectral peak. The spectral decomposition allowed us to classify 3 GPS galaxies as compact symmetric objects (CSO), 1 galaxy and 1 quasar as complex (CX) sources, 2 quasars and 5 galaxies as core-jet (CJ) sources, and 9 galaxies and 2 quasars as compact doubles (CD). The strong morphological dichotomy of GPS galaxies and quasars found by Stanghellini et al. (1997) in their radio bright GPS sample is not so clear in this sample. However, many of the sources classified as CD and CJ have a two-component structure, making their classification only tentative.

ACKNOWLEDGEMENTS

The authors are grateful to the staff of the EVN and VLBA for support of the observing projects. The VLBA is an instrument of the National Radio Astronomy Observatory, which is operated by Associated Universities, Inc. under a Cooperative Agreement with the National Science Foundation. This research was supported by the European Commission, TMR Access to Large-scale Facilities programme under contract No. ERBFMGECT950012, and TMR Programme, Research Network Contract ERBFMRXCT96-0034 "CERES".

REFERENCES

- Conway J.E., Pearson T.J., Readhead A.C.S., Unwin S.C., Xu W., Mutel R.L. 1992, *Ap. J.*, **396**, 62
- Dallacasa D., Fanti C., Fanti R., Schilizzi R.T., Spencer R.E., 1995 *Astron. Astrophys.*, **295**, 27
- Henstock D.R., Browne I.W.A., Wilkinson P.N., Taylor G.B., Vermeulen R.C., Pearson T.J., Readhead A.C.S, 1995 *Astrophys. J. Suppl.*, **100**, 1
- O'Dea C.P., Baum S.A., Stanghellini C., 1991, *Astrophys. J.*, **380**, 66
- O'Dea C.P., 1998, P.A.S.P., bf 110, 493
- Owsianik I. and Conway J.E., 1998, *Astron. & Astrophys.*, **337**, 69
- Owsianik I., Conway J.E., and Polatidis A.G., 1998, *Astron. & Astrophys.*, **336**, L37
- Perlman E.S., Stocke J.T., Shaffer D.B., Carilli C.L., Ma C., 1994, *ApJ*, 424, 69
- Philips R.B. and Mutel R.L., 1982, *Astrophys. J.*, **236**, 89
- Polatidis A.G. Wilkinson P.N., Readhead A.C.S, Pearson T.J., Taylor G.B., Vermeulen R.C., 1995, *Astrophys. J. Suppl.*, **98**, 1
- Rengelink R.B., Tang Y., de Bruyn A.G., Miley G.K., Bremer M.N., Röttgering H.J.A., Bremer M.A.R., 1997, *Astr. & Astrophys.*, in press
- Schwab F.R. and Cotton W.D., 1983, *Astron. J.*, **88**, 688
- Snellen, I.A.G., Schilizzi R.T., de Bruyn A.G., Miley G.K., Rengelink R.B., Röttgering H.J.A., Bremer M.N., 1998a, *A&AS.*, **131**, 435
- Snellen, I.A.G., Schilizzi R.T., de Bruyn A.G., Miley G.K., 1998a, *A&A*, 333, 70

- Snellen I.A.G., Schilizzi R.T., Bremer M.N., de Bruyn A.G., Miley G.K., Röttgering H.J.A., McMahon R.G., Pérez Fournon I., 1998b, *M.N.R.A.S.*, **301**, 985
- Snellen, I.A.G., Schilizzi R.T., de Bruyn A.G., Miley G.K., 1998c, *A&A*, 333, 70
- Snellen I.A.G., Schilizzi R.T., Bremer M.N., Miley G.K., de Bruyn A.G., Röttgering H.J.A., 1999, *M.N.R.A.S.*, **307**, 139
- Snellen I.A.G., Schilizzi R.T., Miley G.K., de Bruyn A.G., Bremer M.N., Röttgering H.J.A., *M.N.R.A.S.* submitted (companion paper)
- Staghellini C., O’Dea C.P., Baum S.A., Dallacasa D., Fanti R., Fanti C., *Astron. & Astrophys.*, 1997, **325**, 943
- Taylor G.B. and Vermeulen R.C., 1997, *Astrophys. J.*, **485**, L9
- van Breugel, W., Miley, G., and Heckman, T., *Astron. J.*, **89**, 5
- Wilkinson, P. N., Booth, R. S., Cornwell, T. J., Clark, R. R. 1984, *Nature*, **308**, 619
- Wilkinson, P. N., Polatidis, A. G., Readhead, A. C. S., Xu, W., Pearson, T. J. 1994, *Astrophys. J.*, **432**, L87

Name	1.6 GHz Map Parameters				5 GHz Map Parameters				15 GHz Map Parameters			
	Beam (mas)	°	rms $\frac{\mu Jy}{beam}$	S_{peak} $\frac{mJy}{beam}$	Beam (mas)	°	rms $\frac{\mu Jy}{beam}$	S_{peak} $\frac{mJy}{beam}$	Beam (mas)	°	rms $\frac{\mu Jy}{beam}$	S_{peak} $\frac{mJy}{beam}$
0400+6042					1.2×1.1	65.8	180	38	1.1×0.6	-22.4	280	34
0436+6152	5.6×2.5	-26.3	120	110	3.4×1.2	68.5	230	42	1.3×1.1	-35.3	200	25
0441+5757					2.3×1.3	70.5	200	96	1.6×1.2	-70.2	230	73
0513+7129					1.4×0.9	14.2	190	51	0.8×0.7	41.0	170	52
0531+6121					2.0×1.0	24.0	130	19	1.2×1.0	-46.4	270	30
0535+6743	9.7×3.7	-5.8	416	89	1.6×1.0	10.3	230	148	1.4×1.2	45.9	200	71
0537+6444	9.3×3.7	-10.6	85	29	2.2×1.0	12.8	190	13				
0538+7131					1.5×1.1	13.4	170	73	1.9×1.6	-51.5	310	30
0539+6200	4.4×2.9	-2.6	550	83	1.9×1.0	22.4	170	91	0.8×0.5	56.9	290	95
0543+6523	3.8×3.0	-11.6	240	50	1.7×1.1	23.1	170	32				
0544+5847					1.9×1.0	-7.1	210	19				
0552+6017	4.3×2.9	-7.4	120	40	2.1×0.9	3.4	350	8				
0557+5717	4.7×3.0	3.7	90	39	1.4×0.9	-11.7	150	10				
0601+5753					1.5×1.0	-1.5	210	147	1.5×0.9	-44.7	380	73
0748+6343					1.5×1.0	15.1	270	124				
0752+6355					1.0×0.9	19.1	150	152	0.7×0.5	-18.4	330	104
0755+6354					2.8×1.9	12.8	340	14	0.7×0.5	11.8	280	20
0756+6647					2.2×1.1	46.3	130	94	0.7×0.5	-33.5	270	63
0758+5929	4.6×2.6	-18.2	149	144	2.5×1.2	20.1	170	116	1.3×0.5	13.5	200	62
0759+6557	4.1×2.9	-4.7	140	24	1.9×1.1	-27.1	220	10				
0826+7045					1.3×1.2	15.1	190	85				
0830+5813	4.3×2.5	-15.7	107	44	1.6×1.1	9.0	180	29				
1525+6801	4.3×3.2	-72.0	170	109	1.1×1.0	7.0	120	48	1.4×1.4	-29.8	230	23
1538+5920					2.7×1.2	0.4	140	42	0.5×0.5	0.0	350	11
1550+5815					2.6×1.2	-0.4	170	198	1.2×0.4	15.8	360	120
1551+6822	4.4×3.2	-65.4	130	46	3.3×1.3	6.2	160	20				
1557+6220	4.4×2.8	6.6	76	34	2.7×1.1	-2.8	240	15				
1600+7131	3.9×3.1	64.3	110	161	2.3×1.5	68.6	170	45	0.6×0.5	-40.0	190	26
1620+6406	3.9×3.3	63.3	110	27	3.6×3.3	-33.4	370	12				
1622+6630					2.9×1.2	-28.7	150	198	0.8×0.5	16.6	290	138
1639+6711	4.1×2.7	13.3	72	57	2.1×1.1	0.1	140	28				
1642+6701	3.9×3.2	72.2	120	62	1.4×0.9	13.9	110	19				
1647+6225	4.0×3.3	36.5	130	25	3.6×3.1	-33.2	190	15				
1655+6446	3.7×3.2	1.6	140	31	3.1×2.0	-28.5	310	14				
1657+5826	3.9×3.2	1.0	110	30	3.8×2.1	38.0	260	14				
1746+6921	5.3×3.0	20.6	75	91	1.5×1.0	2.1	180	86	1.0×0.7	-76.8	350	63
1807+5959	4.1×3.4	-89.8	110	14	2.5×1.0	3.2	170	26				
1807+6742	3.9×3.2	80.4	120	25	4.8×3.6	50.1	310	14				
1808+6813	4.1×2.8	19.9	59	18	2.6×0.8	-4.1	200	17				
1819+6707	3.9×3.2	57.3	150	67	2.5×1.1	46.1	180	22	0.9×0.7	-21.7	260	27
1841+6715	3.9×3.2	84.4	170	120	2.8×1.1	35.0	180	104	1.3×1.0	15.1	300	57
1843+6305	4.0×3.3	83.3	150	46	3.0×0.9	9.7	200	20				
1942+7214	3.9×2.8	33.5	65	161	3.3×1.6	15.2	250	172	0.7×0.5	23.2	310	84
1945+6024					2.7×1.1	-3.7	170	73	0.9×0.5	22.8	310	78
1946+7048	3.9×3.3	-79.7	250	305	1.0×0.9	-28.6	180	84	1.6×1.1	28.6	240	70
1954+6146					2.5×1.2	-1.6	210	142	0.8×0.5	2.9	360	89
1958+6158					2.5×1.1	0.0	240	111	1.2×0.6	-13.4	380	60

Table 2. Relevant parameters of the presented maps.

Name	Fg	Cp	1.6 GHz Data					5.0 GHz Data					14.9 GHz Data				
			Flx mJy	ΔX mas	ΔY mas	Size mas	PA °	Flx mJy	ΔX mas	ΔY mas	Size mas	PA °	Flx mJy	ΔX mas	ΔY mas	Size mas	PA °
0400+6042	2	E						62.7 \pm 3.1	0.0	0.0	1.8 \times 1.2	140	58.5 \pm 2.9	0.0	0.0	1.3 \times 0.2	153
		W						11.0 \pm 0.6	4.1	1.7	2.2 \times 1.7	71	1.9 \pm 0.2	4.1	1.7	—	0
		W						2.8 \pm 0.2	1.2	1.2	< 0.2	0	6.1 \pm 0.4	1.2	1.2	—	0
		W						3.3 \pm 0.3	2.0	1.2	< 0.1	0	2.3 \pm 0.2	2.0	1.2	—	0
0436+6152	1	S	169 \pm 8	0.0	0.0	3.1 \times 0.9	41	84.7 \pm 4.2	0.0	0.0	2.9 \times 0.9	38	7.2 \pm 0.4	0.0	0.0	2.7 \times 0.8	41
		C	36.8 \pm 1.9	-2.8	4.8	1.5 \times 0.6	67	37.3 \pm 1.9	-3.2	5.0	1.4 \times 0.8	64	25.5 \pm 1.3	-3.0	4.8	0.2 \times 0.1	50
		C											2.2 \pm 0.2	-3.7	6.4	1.5 \times 0.5	43
		C											2.8 \pm 0.2	-1.8	3.2	1.2 \times 0.8	66
		N	3.1 \pm 0.3	-5.2	10.5	< 1.2	0	2.2 \pm 0.2	-5.9	11.4	1.8 \times 0.8	50	4.4 \pm 0.3	-5.7	9.5	2.0 \times 0.5	32
		N	4.3 \pm 0.3	-8.4	14.9	9.3 \times 2.9	21										
0441+5757	2	C						111 \pm 5	0.0	0.0	1.0 \times 0.5	45	73.9 \pm 3.7	0.0	0.0	< 0.1	0
0513+7129	2	N						64.7 \pm 3.2	0.0	0.0	0.8 \times 0.5	34	54.7 \pm 2.7	0.0	0.0	< 0.1	0
		S						60.4 \pm 3.0	-0.7	-3.5	1.2 \times 0.6	33	18.6 \pm 1.0	-0.6	-3.6	< 0.1	0
		W						4.2 \pm 0.3	2.0	1.1	—	0					
		W						2.0 \pm 0.2	2.9	1.4	—	0					
		W						3.7 \pm 0.3	4.8	2.3	—	0	2.5 \pm 0.2	5.1	1.8	1.5 \times 0.6	65
		W						2.6 \pm 0.2	6.4	3.4	—	0					
0531+6121	2	C						18.7 \pm 1.0	0.0	0.0	< 0.2	0	30.1 \pm 1.5	0.0	0.0	0.2 \times 0.1	142
0535+6743	1	C	94.5 \pm 4.7	0.0	0.0	4.0 \times 1.9	165	166 \pm 8	0.0	0.0	0.5 \times 0.4	174	78.8 \pm 3.9	0.0	0.0	0.5 \times 0.4	94
0537+6444	2	C	31.9 \pm 1.6	0.0	0.0	1.8 \times 0.9	9	15.3 \pm 0.8	0.0	0.0	1.3 \times 0.2	12					
		C						1.3 \pm 0.2	1.1	-4.7	—	0					
0538+7131	2	C						78.0 \pm 3.9	0.0	0.0	0.5 \times 0.3	152	29.6 \pm 1.5	0.0	0.0	< 0.2	0
0539+6200	1	W	96.8 \pm 4.8	0.0	0.0	1.7 \times 1.2	126	101 \pm 5	0.0	0.0	0.6 \times 0.4	163	95.0 \pm 4.8	0.0	0.0	< 0.2	0
		E	10.3 \pm 0.6	-4.6	4.0	2.7 \times 0.8	121	4.3 \pm 0.3	-4.8	2.8	3.3 \times 1.8	36					
0543+6523	2	C	62.7 \pm 3.1	0.0	0.0	2.1 \times 1.3	90	36.8 \pm 1.9	0.0	0.0	0.7 \times 0.5	36					
		C						5.2 \pm 0.3	2.5	-0.6	1.2 \times 0.5	36					
0544+5847	3	C						18.6 \pm 1.0	0.0	0.0	0.4 \times 0.1	175					
		C						7.9 \pm 0.4	0.6	1.6	0.7 \times 0.4	21					
		C						1.4 \pm 0.2	1.3	4.7	< 1.1	0					
		C						3.0 \pm 0.2	1.6	8.0	1.8 \times 0.7	173					
0552+6017	2	C	41.8 \pm 2.1	0.0	0.0	0.9 \times 0.2	71	13.6 \pm 0.7	0.0	0.0	1.5 \times 0.3	114					
		C	1.2 \pm 0.2	-12.2	-3.3	< 1.7	0										
0557+5717	2	N	49.2 \pm 2.5	0.0	0.0	2.5 \times 1.2	44	12.5 \pm 0.7	0.0	0.0	3.1 \times 1.5	42					
		S	10.9 \pm 0.6	3.0	-5.8	2.3 \times 1.5	124	16.3 \pm 0.8	2.2	-8.9	3.4 \times 1.8	18					
0601+5753	2	C						188 \pm 9	0.0	0.0	0.8 \times 0.3	106	94.9 \pm 4.7	0.0	0.0	0.9 \times 0.3	98
0748+6343	3	C						126 \pm 6	0.0	0.0	0.2 \times 0.1	65					
0752+6355	2	C						182 \pm 9	0.0	0.0	1.2 \times 0.2	167	31.6 \pm 1.6	0.0	0.0	0.4 \times 0.1	144
		S						105 \pm 5	0.3	-0.5	1.9 \times 0.5	24	62.3 \pm 3.1	0.3	-0.5	0.8 \times 0.3	24
		N						17.4 \pm 0.9	0.3	0.7	< 0.8	0	108 \pm 5	0.3	0.7	0.2 \times 0.1	142
		W						2.4 \pm 0.2	1.8	1.5	—	0					
		W						4.6 \pm 0.3	4.2	1.8	—	0					
		C						19.9 \pm 1.0	0.0	0.0	0.7 \times 0.2	132	19.9 \pm 1.0	0.0	0.0	< 0.1	0
0755+6354	2	C						98.1 \pm 4.9	0.0	0.0	0.4 \times 0.3	34	72.6 \pm 3.6	0.0	0.0	0.3 \times 0.2	29
0758+5929	1	W	122 \pm 6	0.0	0.0	—	0	121 \pm 6	0.0	0.0	0.8 \times 0.2	36	76.4 \pm 3.8	0.0	0.0	0.7 \times 0.2	31
0759+6557	2	E	71.4 \pm 3.6	-1.7	1.0	—	0	34.1 \pm 1.7	-1.8	0.9	0.6 \times 0.5	41	10.4 \pm 0.6	-1.9	0.8	0.6 \times 0.3	12
		W	25.5 \pm 1.3	0.0	0.0	0.9 \times 0.6	3	12.6 \pm 0.7	0.0	0.0	0.9 \times 0.6	154					
		E	17.8 \pm 0.9	-4.8	-5.6	1.7 \times 1.4	62	4.1 \pm 0.3	-5.5	-5.8	1.3 \times 1.0	23					
0826+7045	3	E						1.8 \pm 0.2	-3.0	-5.3	1.7 \times 1.4	142					
		C						90.5 \pm 4.5	0.0	0.0	0.4 \times 0.2	162					
		C	50.8 \pm 2.5	0.0	0.0	1.9 \times 1.0	0	39.6 \pm 2.0	0.0	0.0	0.6 \times 0.5	66					
0830+5813	2	C						80.9 \pm 4.0	0.0	0.0	1.1 \times 0.6	151	24.4 \pm 1.2	0.0	0.0	0.4 \times 0.2	171
1525+6801	1	S	137 \pm 6	0.0	0.0	2.5 \times 1.1	170	8.5 \pm 0.5	13.2	18.1	1.5 \times 0.8	170	3.9 \pm 0.3	12.7	18.4	2.9 \times 0.9	22
		N	14.5 \pm 0.8	13.1	17.8	2.1 \times 1.2	166	5.8 \pm 0.4	11.5	16.3	2.4 \times 1.9	112					
		N	15.6 \pm 0.8	10.2	13.7	5.4 \times 3.4	135	2.3 \pm 0.2	10.4	13.4	1.6 \times 0.3	36					
1538+5920	2	C						45.9 \pm 2.3	0.0	0.0	0.7 \times 0.3	27	20.1 \pm 1.0	0.0	0.0	0.7 \times 0.3	20
1550+5815	2	C						233 \pm 11	0.0	0.0	1.4 \times 0.2	158	174 \pm 8	0.0	0.0	0.7 \times 0.2	164
1551+6822	2	C	49.6 \pm 2.5	0.0	0.0	1.7 \times 0.5	105	21.1 \pm 1.1	0.0	0.0	< 0.3	0					
		C						5.1 \pm 0.3	-2.3	-0.9	< 1.0	0					
1557+6220	2	C	39.3 \pm 2.0	0.0	0.0	1.5 \times 0.8	89	17.9 \pm 0.9	0.0	0.0	1.2 \times 0.4	156					

Table 3. The fitted parameters of the observed components.

Name	Fg	Cp	1.6 GHz Data					5.0 GHz Data					14.9 GHz Data				
			Flx mJy	ΔX mas	ΔY mas	Size mas	PA °	Flx mJy	ΔX mas	ΔY mas	Size mas	PA °	Flx mJy	ΔX mas	ΔY mas	Size mas	PA °
1557+6220	2	C	39.3±2.0	0.0	0.0	1.5×0.8	89	17.9±0.9	0.0	0.0	1.2×0.4	156					
1600+7131	1	N	261±13	0.0	0.0	3.1×2.2	124	54.4±2.7	0.0	0.0	1.0×0.7	47	26.3±1.3	0.0	0.0	< 0.1	0
		N						19.8±1.0	-1.4	-1.7	2.4×1.4	110					
		N						4.0±0.3	2.6	-3.6	< 1.4	0					
		S	8.3±0.5	4.7	-22.2	2.2×1.2	115	6.7±0.4	7.7	-20.9	1.5×1.2	141					
		S	15.9±0.8	8.2	-19.3	1.9×1.4	165										
1620+6406	2	N	29.0±1.5	0.0	0.0	1.1×0.8	142	12.9±0.7	0.0	0.0	1.0×0.8	170					
		S	5.2±0.3	0.3	-14.2	< 1.2	0										
1622+6630	2	C						218±10	0.0	0.0	0.6×0.2	60	169±8	0.0	0.0	0.3×0.2	122
1639+6711	2	C	68.5±3.4	0.0	0.0	1.8×0.9	92	38.6±1.9	0.0	0.0	1.0×0.7	69					
1642+6701	2	W	83.4±4.2	0.0	0.0	3.5×0.5	86	14.8±0.8	0.0	0.0	1.3×0.3	76					
		C	8.7±0.5	-4.9	0.0	< 0.8	0	36.8±1.9	-2.7	0.3	1.5×0.4	87					
		E	7.8±0.4	-9.6	0.1	5.1×0.9	99	9.8±0.5	-5.8	0.5	2.1×0.6	79					
1647+6225	2	N	24.2±1.2	0.0	0.0	< 0.4	0	15.8±0.8	0.0	0.0	0.7×0.5	65					
		N	7.0±0.4	4.1	-2.0	2.9×1.0	81										
		S	16.1±0.8	10.0	-12.0	1.9×0.7	76	2.7±0.2	10.5	-12.3	0.8×0.3	19					
1655+6446	2	S	38.5±1.9	0.0	0.0	2.2×1.1	76	18.2±0.9	0.0	0.0	2.0×1.0	108					
		N2	10.2±0.5	-4.7	5.1	< 2.1	0										
		N	2.6±0.2	-19.8	15.0	2.1×1.3	0										
1657+5826	2	S	34.6±1.7	0.0	0.0	1.4×1.4	90	20.2±1.0	0.0	0.0	1.9×1.6	31					
		N	4.2±0.3	-27.0	6.8	< 2.8	0										
1746+6921	1	W	135.3±3.4	0.0	0.0	2.7×0.9	116	102±5	0.0	0.0	—	0	70.8±3.5	0.0	0.0	0.5×0.1	105
		C						50.3±2.5	-1.1	-0.5	—	0	12.5±0.7	-1.2	-0.4	1.4×0.2	129
		E	2.5±0.2	-7.4	-4.3	7.6×2.1	149										
1807+5959	2	S	27.2±1.4	0.0	0.0	1.1×0.4	173	29.3±1.5	0.0	0.0	1.1×0.1	8					
		C	6.0±0.4	0.1	4.8	2.1×1.9	39	1.5±0.2	-0.2	6.3	< 0.8	0					
		N	12.5±0.7	-0.6	12.4	4.7×1.4	6	4.0±0.3	-0.6	13.0	3.8×0.8	9					
1807+6742	2	S	26.5±1.3	0.0	0.0	1.1×0.7	104	5.0±0.3	0.0	0.0	2.9×2.2	165					
		N	11.5±0.6	1.1	5.9	2.6×0.4	178	14.8±0.8	1.1	6.8	< 0.7	0					
1808+6813	2	C	26.9±1.4	0.0	0.0	3.5×1.2	167	19.0±1.0	0.0	0.0	< 0.7	0					
1819+6707	1	E	123±6	0.0	0.0	4.6×2.2	58	70.2±3.5	0.0	0.0	3.7×1.6	51	56.2±2.8	0.0	0.0	1.2×0.6	90
		E											9.1±0.5	-2.6	2.1	< 0.2	0
		E						4.7±0.3	3.2	1.6	3.5×1.5	32					
		C	4.7±0.3	7.0	1.8	—	0	5.7±0.3	8.6	2.0	2.6×2.0	96					
		W	66.5±3.3	16.0	4.8	6.4×4.3	112	14.6±0.8	15.0	3.3	4.4×2.3	58					
		W	52.9±2.7	18.6	4.8	4.2×2.1	33	41.4±2.1	18.0	5.2	4.2×1.9	38	7.9±0.4	25.5	8.3	< 0.1	0
		W											4.4±0.3	27.2	7.3	< 0.2	0
		W											2.6±0.2	28.1	6.5	< 0.2	0
1841+6715	1	S	127±6	0.0	0.0	1.0×0.8	126	123±6	0.0	0.0	0.8×0.5	169	67.3±3.4	0.0	0.0	0.5×0.4	142
		N	17.8±0.9	1.4	5.2	2.5×1.9	132	5.2±0.3	1.7	5.9	1.0×0.9	71	2.6±0.2	2.3	6.9	< 0.4	0
1843+6305	2	S	50.1±2.5	0.0	0.0	1.4×0.7	156	26.7±1.3	0.0	0.0	1.1×0.7	177					
		N	17.8±0.9	2.6	8.9	2.3×0.6	59	7.0±0.4	2.6	9.1	1.6×1.0	17					
1942+7214	1	N	176±8	0.0	0.0	1.4×0.8	58	173±8	0.0	0.0	0.5×0.4	3	101±5	0.0	0.0	0.4×0.3	14
		C	3.5±0.3	6.1	-11.0	—	36	1.5±0.2	4.4	-10.8	0.8×0.8	0	2.5±0.2	4.0	-11.8	2.4×0.7	55
		S	2.0±0.2	6.5	-17.4	—	171										
		S	3.5±0.3	11.7	-29.3	—	6										
1945+6024	2	C						81.3±4.1	0.0	0.0	0.6×0.3	105	79.7±4.0	0.0	0.0	< 0.1	0
1946+7048	1	N	292±14	0.0	0.0	1.6×0.9	61	215±10	0.0	0.0	1.6×1.0	86	106±5	0.0	0.0	1.1×0.6	96
		N	196±9	-3.4	-0.1	7.9×3.0	83	53.0±2.7	-5.9	-0.5	3.0×1.5	95	16.2±0.8	-2.3	-0.6	1.8×1.0	73
		N2	150±7	1.2	-6.6	3.2×1.2	9	81.0±4.1	1.2	-7.0	2.9×0.6	13	40.7±2.0	1.2	-7.1	2.1×0.6	11
		C	66.0±3.3	5.4	-13.3	4.2×1.4	47	33.6±1.7	5.6	-13.5	1.3×0.2	45	17.8±0.9	5.5	-13.2	< 1.0	0
		C						27.6±1.4	7.4	-15.2	0.9×0.3	47	66.5±3.3	6.5	-14.5	1.2×0.4	44
		S2	76.4±3.8	10.3	-20.4	3.0×1.2	14	41.4±2.1	10.2	-20.2	1.5×0.5	12	18.2±0.9	9.9	-19.9	1.0×0.5	29
		S	89.8±4.5	13.6	-28.9	5.0×2.6	51	19.9±1.0	13.1	-29.0	3.0×1.1	44					

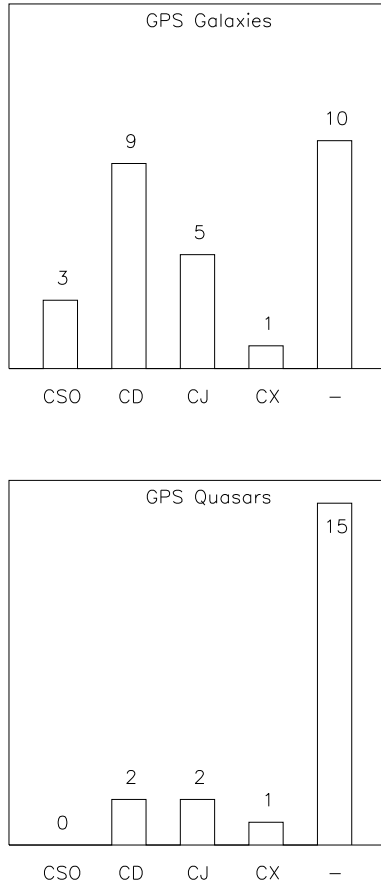


Figure 8. . The number of galaxies and quasars classified as compact symmetric objects (CS0), Compact Doubles (CD), Core-jets (CJ), Complex sources (CX), and sources for which no classification was possible.

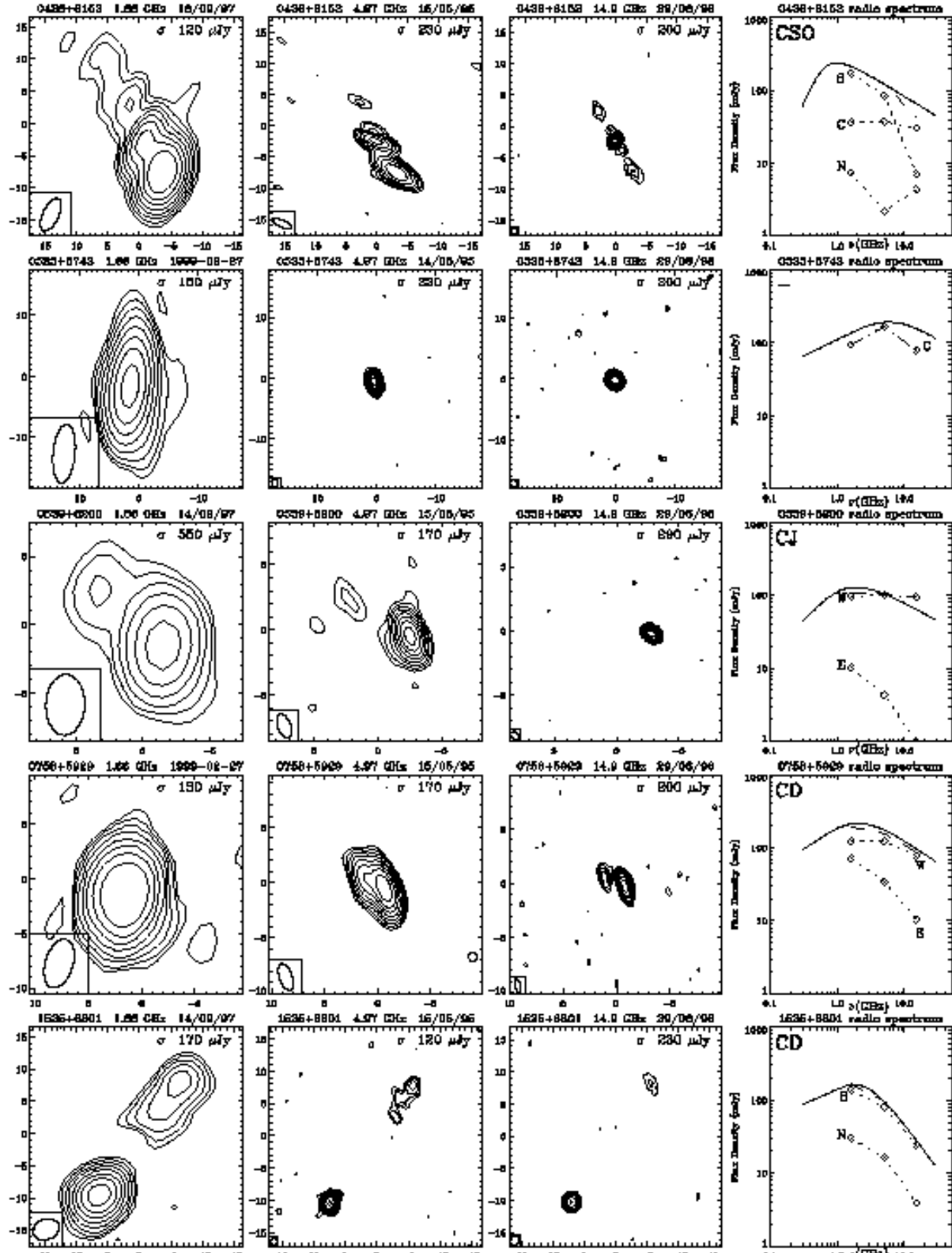


Figure 5. The VLBI maps and spectral decomposition for sources observed at 3 frequencies.

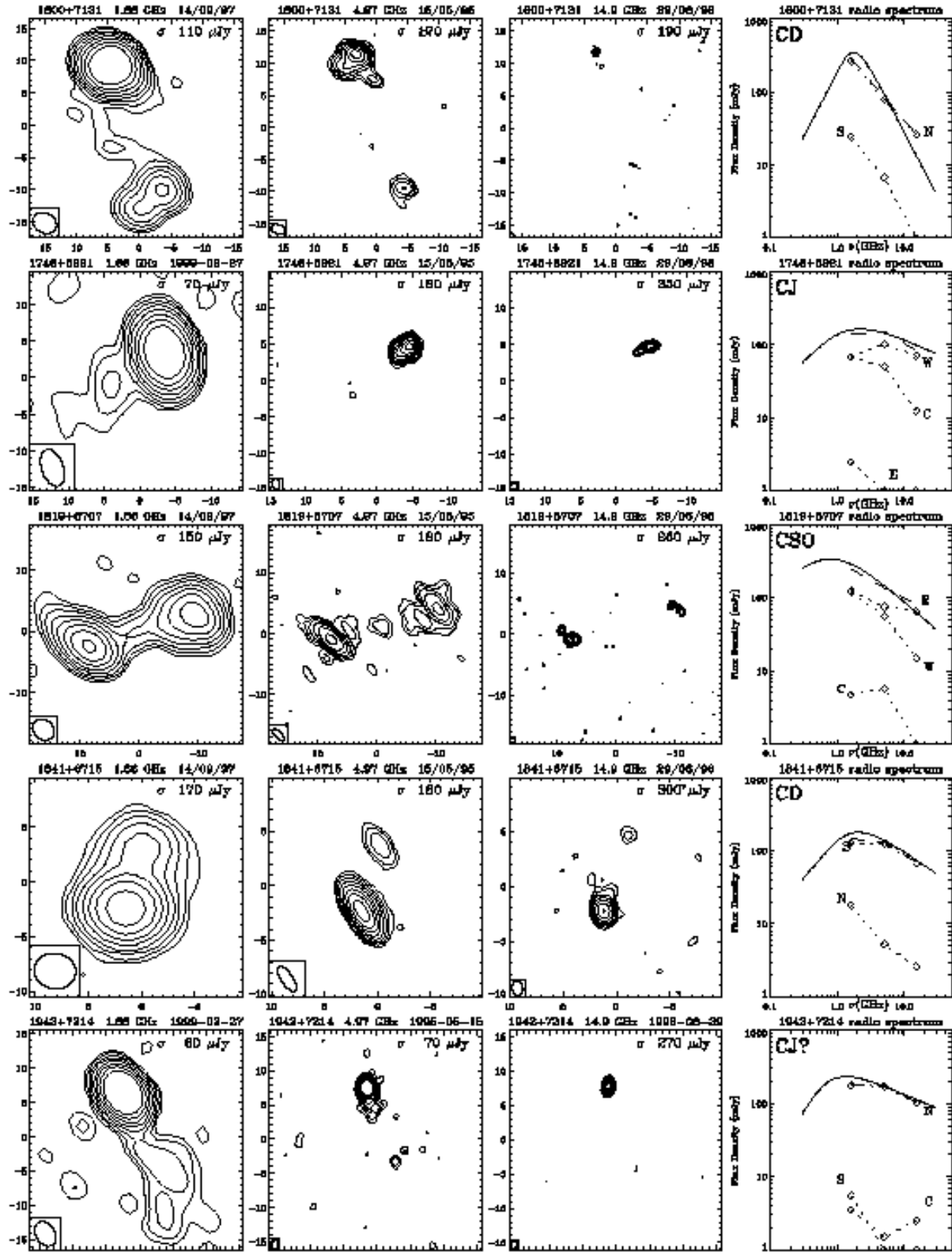


Figure 5. Continued...

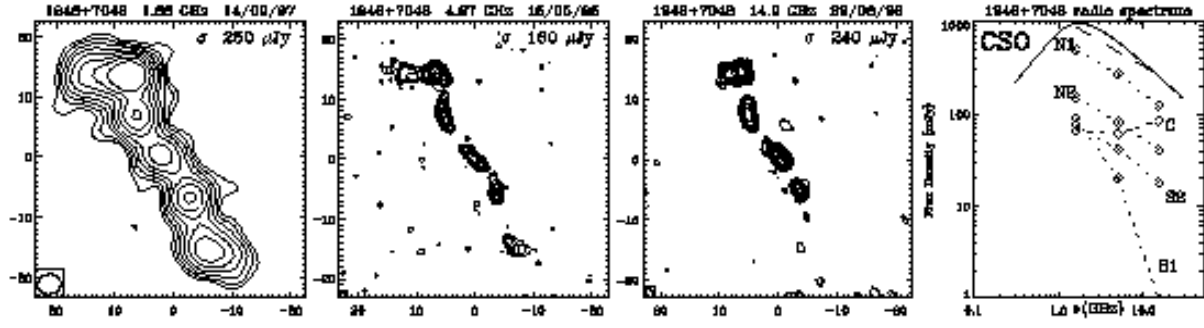


Figure 5. Continued...

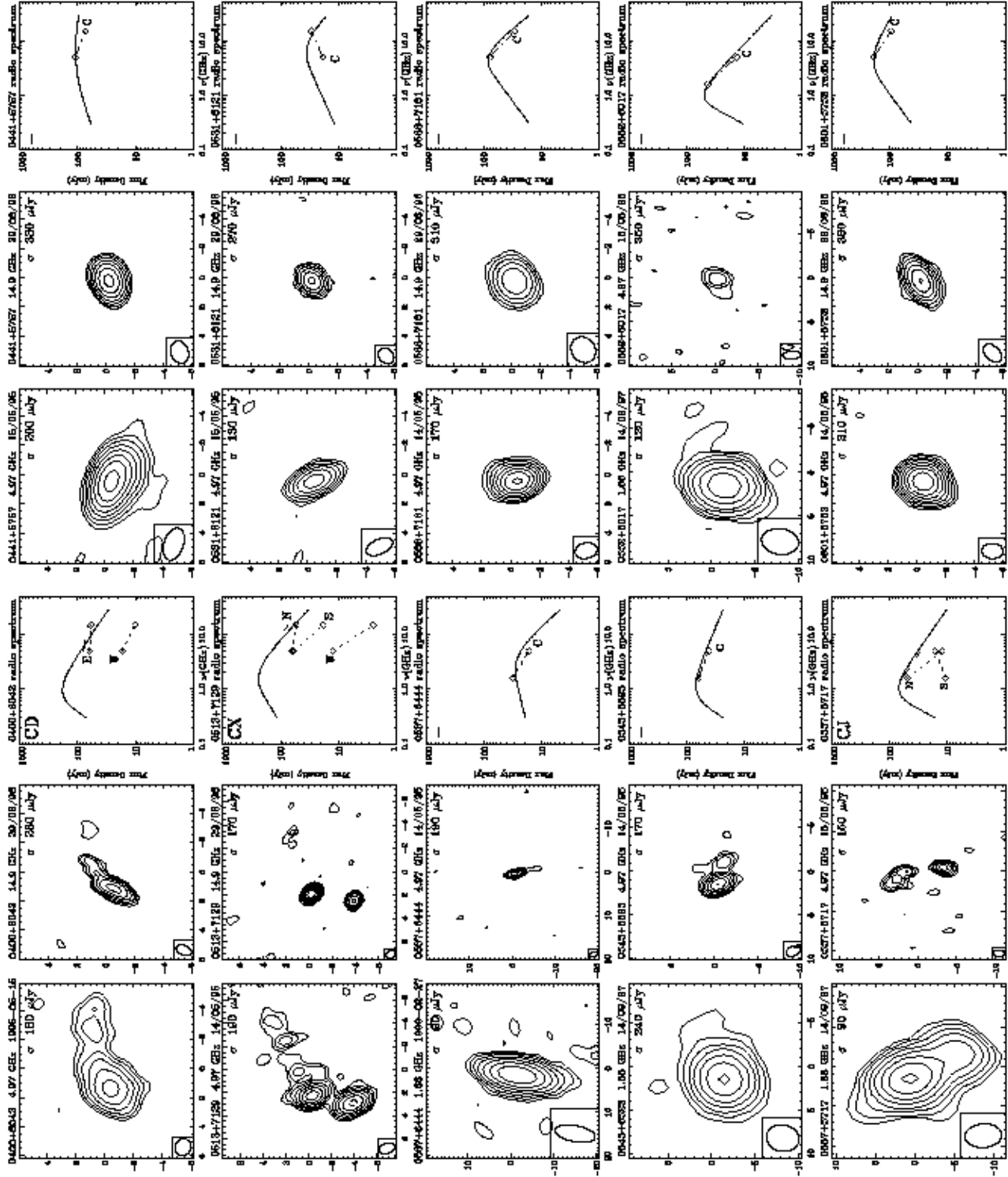


Figure 6. The VLBI maps and spectral decomposition for sources observed at 2 frequencies.

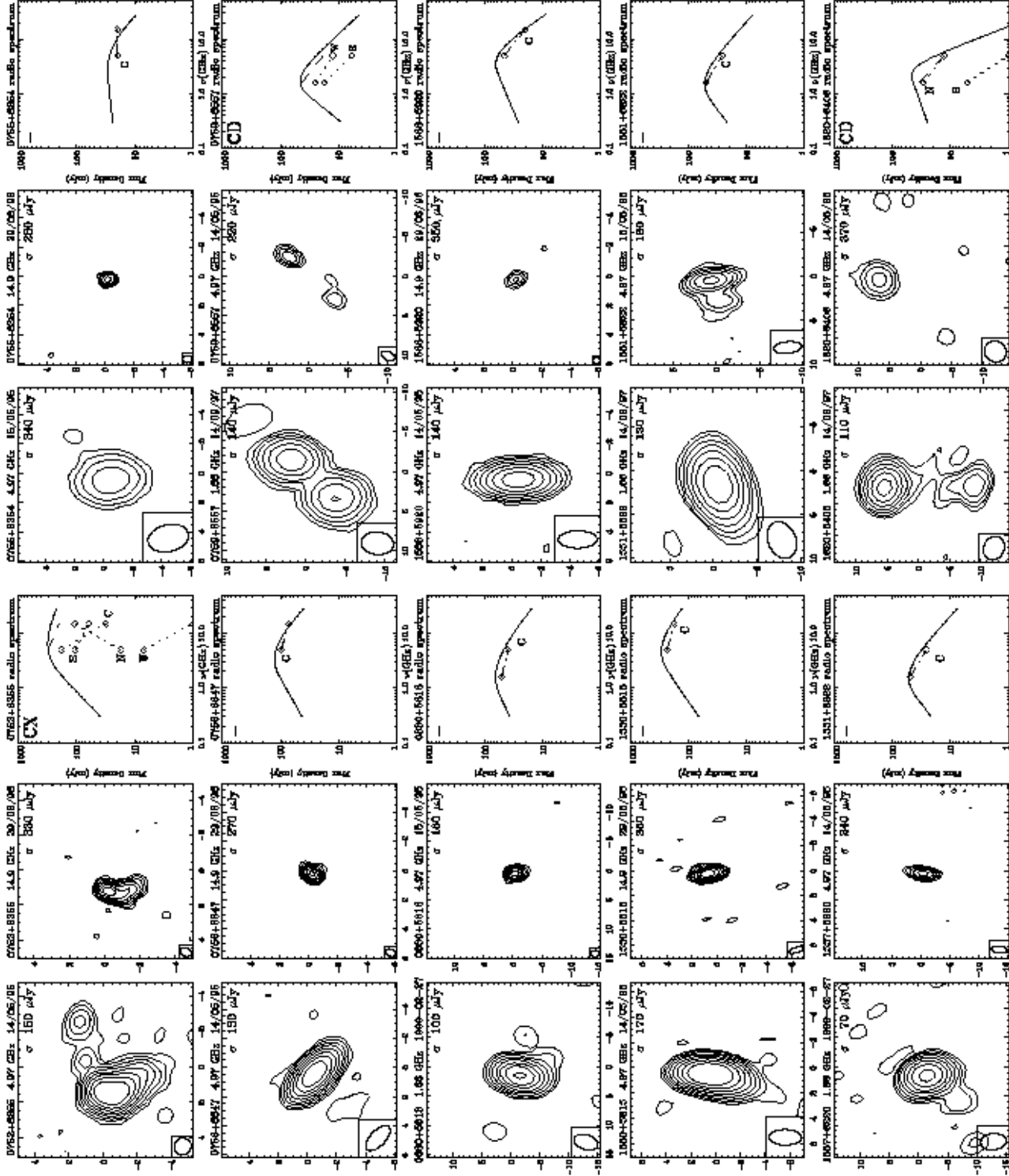


Figure 6. Continued...

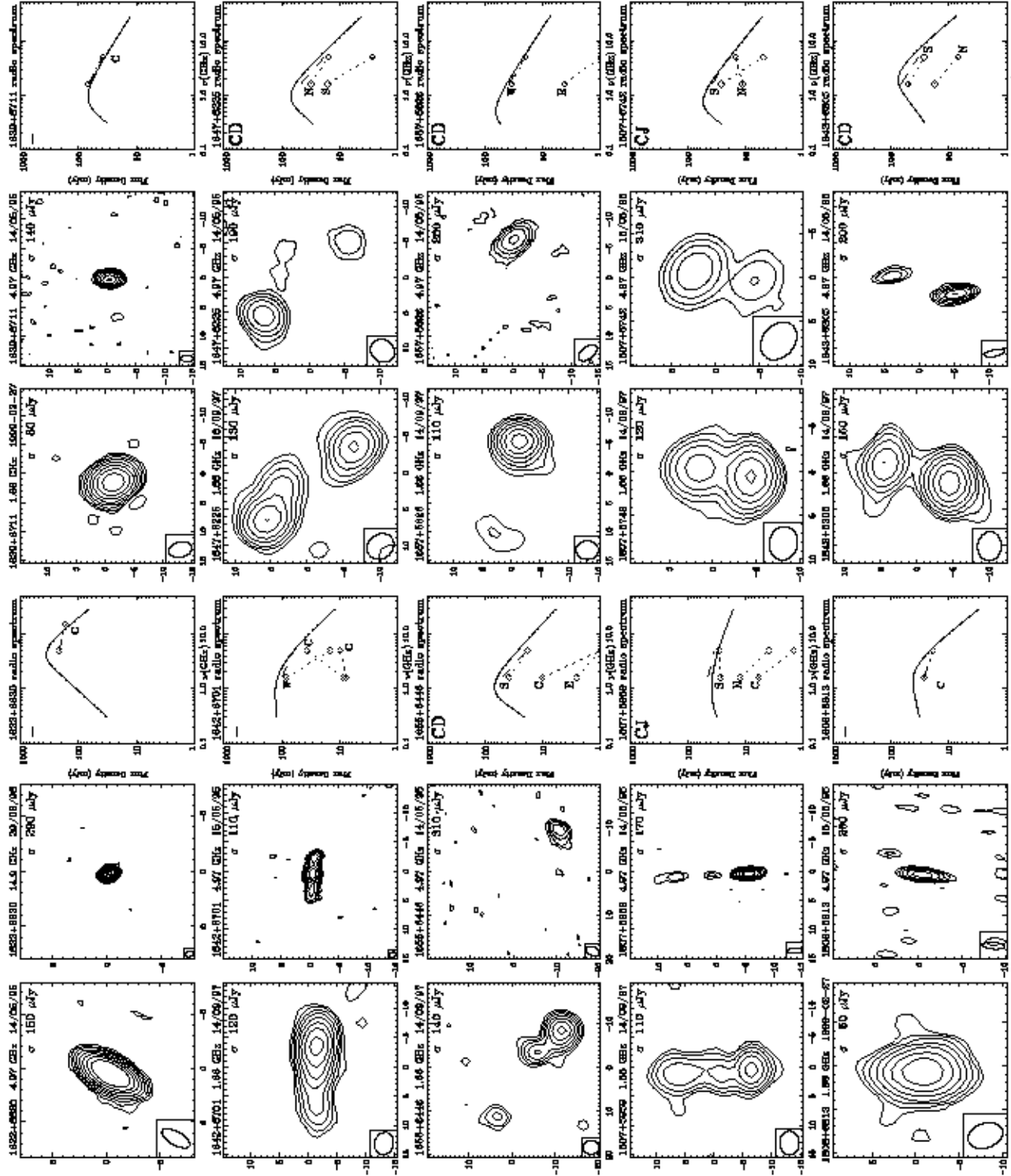


Figure 6. Continued...

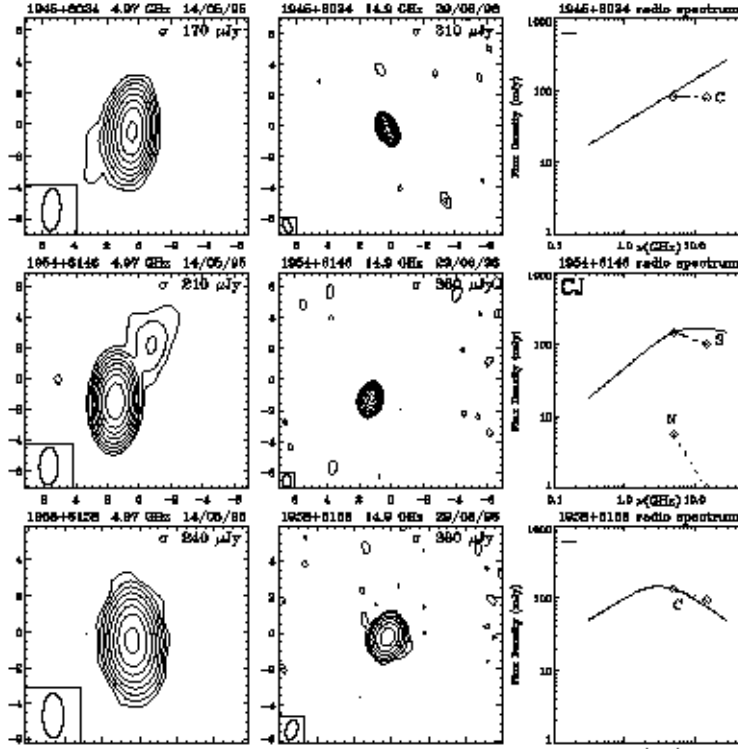


Figure 6. Continued...

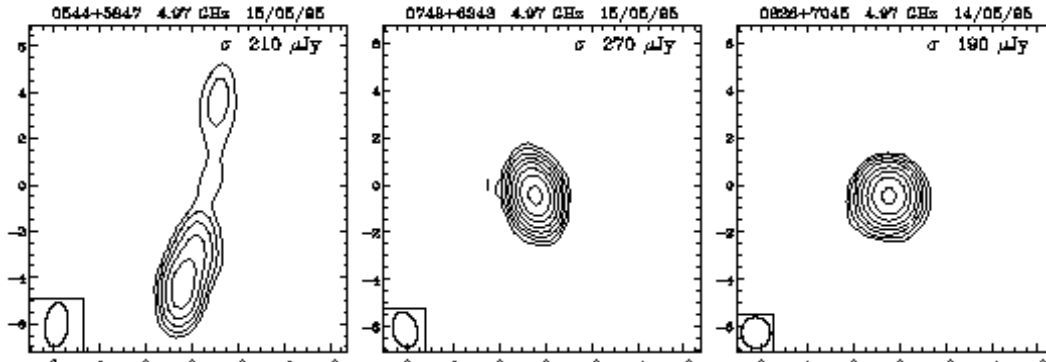


Figure 7. The VLBI maps for the sources observed only at 5 GHz.